

# Topological reconstruction of sub-cellular motion with Ensemble Kalman velocimetry

Le Yin

October 10, 2019

## Abstract

Microscopy image video allows elaborated analysis of sub-cellular motions of organelles in a plant cell. The large data set obtained from the video can be only analyzed by automated algorithms. Here we develop a novel, data-oriented algorithm that can track the organelle movements and reconstruct the trajectories on stacks of image data. This method proceeds with three steps: (i) identification, (ii) localization and (iii) linking. The method combines topological data analysis and Ensemble Kalman Filtering, and it performs without assuming a specific motion model. Application of this method on the simulated data sets show good agreement comparing to its truth underground. We also test the developed method successfully on real data.

**Keywords:** multi-target tracking, velocimetry, topological data analysis, ensemble Kalman filter, fluorescence microscopy

**Running head:** *Kalman velocimetry and motion reconstruction*

## 1 Introduction

Cell physiology depends on the motion of sub-cellular structures and cytosolic streaming or organelle motility are critical factors [5, 6, 12, 38, 49]. Such intracellular motions are particularly pronounced in plant cells and are essential, among other cell functions, also to cell growth and overall health [32]. In particular, organelle motility in plant cells is driven by motor proteins that move directionally along myosin filaments or diffuse in the cell sap and occasionally switch between these modes. Additionally, different motor proteins generate motion patterns with different characteristics such as speeds, turning angles, switching frequencies, etc. Due to the complex nature of the underlying dynamics, an understanding of organelle motility based on first principles remains missing. Instead, intracellular motion is commonly studied experimentally.

Among the most popular techniques employed for the direct observation of intracellular motion is conventional fluorescence microscopy [36, 35, 37, 51]. The highly engineered optical equipment available and the fast development of an array of bio-molecular techniques now allow routine observation of organelle dynamics and the acquisition of vast datasets. A thorough and accurate reconstruction of organelle trajectories in these datasets is a necessary task for distinguishing motor protein structures, elucidating their behavior and characterizing globally their motility. To accomplish this, a couple of studies analyze raw measurements and track sub-cellular motions manually which, in practice, yields acceptable estimates with good accuracy [10, 16, 17]. Nevertheless, manual tracking is tedious, time consuming, unrepeatable and unrealistic for complex datasets, especially those encountered in plant microscopy.

Automated tracking algorithms, capable for analyzing such datasets, provide an opportunity to overcome these difficulties and robustly track a large number of sub-cellular targets. Furthermore, they cannot only overcome the low throughput of manual tracking, but also offer tighter error bounds. Additionally, automated tracking algorithms can reveal large scale motion patterns during the entire time course of an imaging

experiment [11]. Therefore, automated tracking algorithms for organelles, specifically designed for plant cell imaging, are essential.

Intracellular tracking can be broken down into four steps: (i) identification, where the number of moving organelles is estimated first; (ii) localization, where the position of each identified organelle is detected in space and throughout time; (iii) linking, where estimated localizations belonging to the same organelle trajectory are connected over time; and (iv) interpretation, where the estimated trajectories are used to derive quantitative information about the organelle motion [27]. Many studies about multiple targets tracking has been developed so far [1, 4, 25, 32, 33, 45, 46, 50], but only few of them are dealing specifically with microscopy image data, while the others are not applicable to image data or failed by introducing misassignment. The study in [32] provide a solution by using a Bayesian framework on the set intracellular movements, [42] solves the problem by considering a topological linking technique with minimal assumptions about the underlying dynamics. In [27], a survey of all techniques applicable to image data is provided in that paper.

With this work, we aim on improving the linking stage. We propose an automated algorithm based on Bayesian identification of organelle parameters, Ensemble Kalman filter (EnKF) estimations of displacement field and topological linking on trajectories space. A Bayesian framework is applied on the parameters of organelles, such as radius, intensity values and locations of the targets. The Bayesian identification yields the best estimation on the image data and experimental measures. We use EnKF to estimate the displacement of organelles since our linking method is based on these displacement. The linking process is completed by using topological data analysis technique [8, 13, 42, 44] to find the geometry of the data space. This allows the data to be embedded into a topological space, in which the trajectories can be reconstructed by identifying connected components.

The structure of this paper is as follows. In next section, we introduce the background needed to establish our algorithm and formulate the problem and give the technical details of the methodology. Section 3 shows the result when apply to two simulated data sets and one real data set. Finally, a discussion and a conclusion with future research directions are presented in section 4.

## 2 Methods

### 2.1 Description of datasets

Datasets that capture the motion of cell organelles through conventional fluorescence microscopy are typically provided in video format [18, 27, 43]. Essentially, each dataset consists of a stack of pixelated images  $\mathcal{D} = \{\mathcal{F}_n, t_n\}_{n=1}^N$ , where each image  $\mathcal{F}_n$  is obtained at time  $t_n$  during the course of an experiment.

Ignoring imaging artifacts caused by finite frame rate, dead time, or rolling shutter [27] that are insignificant on the time- and space-scales involved in plant microscopy [29, 31], in this study we consider images obtained at time levels  $\{t_n\}_n$  that start at the experiment's onset and end with the experiment's conclusion, denoted  $t_1 = 0$  and  $t_N = T$ , respectively. Further, we consider intermediate time levels that remain equidistant  $t_n = (n - 1)\Delta t$ , where  $\Delta t = T/(N - 1)$  is the exposure period used for the acquisition of the images.

In turn, each image  $\mathcal{F}_n$  is an array of intensity values  $\{I_n^p\}_{p=1}^P$  where  $I_n^p$  denotes the intensity [19, 47], recorded at time  $t_n$  of a pixel located at a fixed position  $x^p \in \mathbb{R}^2$ . As usual, we assume that the positions of the pixels  $\{x^p\}_{p=1}^P$  are given and that they are reported in physical units in the same coordinate system as the sample under imaging. Ignoring positioning parallel to the optical axis (i.e. ignoring z-depth), which is not captured in conventional fluorescence microscopy [20, 27, 28], we consider  $\mathbb{R}^2$  as representing any plane perpendicular to the optical axis (for example, without any loss  $\mathbb{R}^2$  can model the focal- or xy-plane).

Depending upon the imaging equipment employed in the experiment (i.e. cameras or other light detectors), intensities may be reported in various forms such as photon or electron counts, voltages, currents,

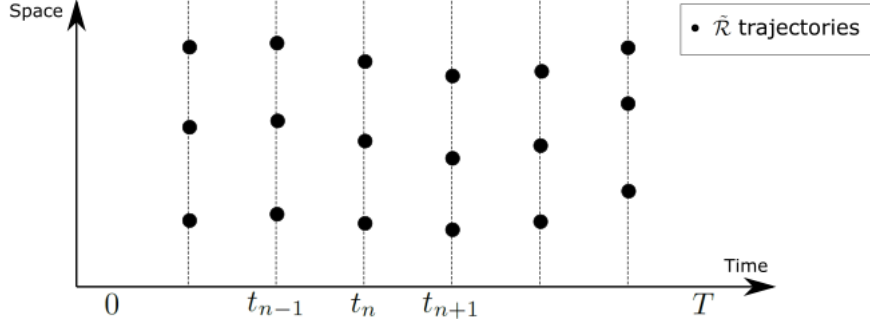


Figure 1: The motion of organelles, during an experiment starting at  $t = 0$  ending at  $t = T$ , is plotted at discrete times  $t_n$  (dots). For simplicity, space is represented with one dimension, although real datasets are two dimensional. The black dots represent the locations of organelles at different time levels.  $\tilde{\mathcal{R}}$  is the set contains the locations of all black dots.

ADUs(Analog Digital Unit), etc [19, 21, 23, 30, 47]. For generality, in this study we assume  $\{I_n^p\}_{n,p}$  are given in normalized gray scale values, i.e.  $I_n^p$  are measured in arbitrary units (a.u.), with the convention that lower intensities correspond to darker pixels and *vice versa* higher intensities correspond to brighter pixels.

To initiate our method, we model each intensity  $I_n^p$  as consisting of a background signal  $B_n^p$ , a signal produced by the organelles in the sample  $J_n^p$ , and noise  $n_n^p$ . That is, we assume

$$I_n^p = B_n^p + J_n^p + n_n^p. \quad (1)$$

To find the locations of organelles, we adopt partial of data preprocessing steps and Bayesian localization step in [42], they are summarized in the following paragraph. In plant microscopy, typically the background signal changes smoothly over and across the frames. Therefore, we model it as a smooth surface over the entire field of view and remove it by least square fitting. In turn, we model the organelle signal as a sum of Gaussian intensity peaks

$$J_n^p = \sum_{s=1}^{\tilde{S}_n} \tilde{h}_n^s \exp \left( -\frac{\|x^p - \tilde{x}_n^s\|^2}{2(\tilde{w}_n^s)^2} \right), \quad (2)$$

where each peak, labeled by  $s$ , is produced by a single organelle [41] that is imaged with maximum intensity  $\tilde{h}_n^s > 0$ , width  $\tilde{w}_n^s > 0$ , and center  $\tilde{x}_n^s \in \mathbb{R}^2$ . We obtain the total number of organelle peaks  $\tilde{S}_n$ , present in each time level  $t_n$ , through thresholding; while we obtain the organelle features  $\{(\tilde{x}_n^s, \tilde{h}_n^s, \tilde{w}_n^s)\}_{s=1}^{\tilde{S}_n}$  through the maximum *a posteriori* estimates [9, 15] of a Bayesian model that assumes: (i) noises  $\{n_n^p\}_p$  are independent and Gaussian, (ii) organelles are *a priori* uniformly positioned over the imaged plane, and (iii) maximum intensities and widths are *a priori* distributed over appropriate finite intervals.

Ignoring imaging artifacts that are caused by intra-frame motion, which are insignificant in plant microscopy [29, 31], we model each localization  $\tilde{x}_n^s \in \mathbb{R}^2$ , as the *effective position* of a single organelle at time  $t_n$ . In other words, following the localization procedure above, we obtain a collection of space-time positions  $\tilde{\mathcal{R}} = \{(\tilde{x}_n^s, t_n)\}_{s=1}^{\tilde{S}_n} \subset \mathbb{R}^2 \times [0, T]$  that reveals the positions of every organelle in the sample only at the experimental time levels  $\{t_n\}_n$ ; see fig. 1.

To proceed with the analysis, we model each organelle's effective position as an idealized point and its motion as a 2D trajectory that ignores positioning parallel to the optical axis which, as we mention above, is not captured in the typical dataset. In other words, each organelle, labeled by  $a$ , in our formulation corresponds to a *continuous* function  $r_a : [0, T] \mapsto \mathbb{R}^2$ , where  $[0, T]$  represents the time course of the experiment and  $\mathbb{R}^2$  represents any plane compatible with the pixel positions  $\{x^p\}_p \subset \mathbb{R}^2$ . Given a dataset  $\mathcal{D}$  of raw experimental

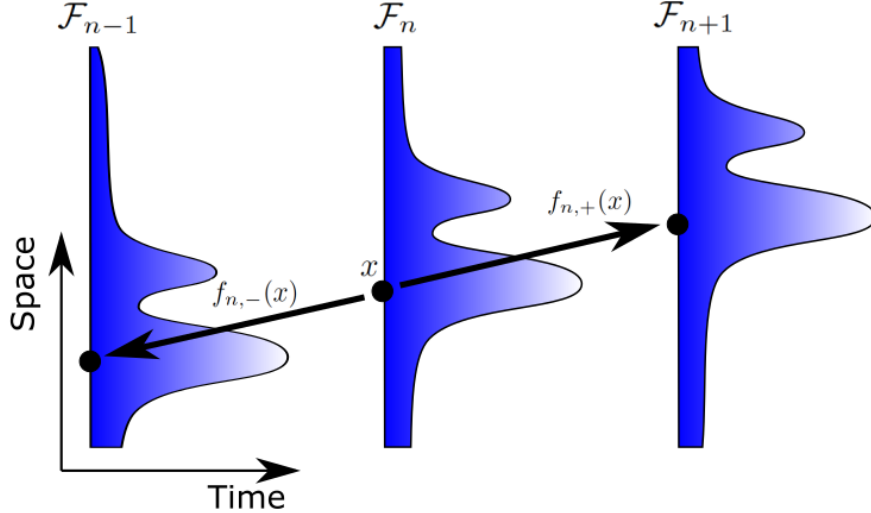


Figure 2: With one dimensional space panel,  $x$  is the position of the organelle with highest intensity value at time  $t_n$ .  $f_{n,+}(x)$  and  $f_{n,-}(x)$  illustrate 1-level forward displacement and backward displacement of  $x$ , respectively.

observations and a collection of organelle space-time localizations  $\tilde{\mathcal{R}}$  identified as described above, our main objective from now on is the computational reconstruction of  $\{r_a\}_a$ .

## 2.2 Kalman velocimetry

The motion of the entire set of organelles in the experiment can be encoded within a family of displacement fields  $f_{t \rightarrow t'}(\cdot) : \mathbb{R}^2 \mapsto \mathbb{R}^2$ , which we use (see Sect. 2.3, below) to distinguish space-time positions that are visited by the same organelle. We adopt functional notation and we write  $f_{t \rightarrow t'}(\cdot)$  to emphasize that these variables are entire functions, in contrast to writing  $f_{t \rightarrow t'}(x)$ , which is a point, or simply  $f_{t \rightarrow t'}$ , which might be confused with the other scalar or vector-valued variables in our formulation.

In particular, according to our convention, for any organelle, its position  $x \in \mathbb{R}^2$  at a time  $t \in [0, T]$  and its position  $x' \in \mathbb{R}^2$  at a time  $t' \in [0, T]$  are coupled by the displacement fields as

$$x' = x + f_{t \rightarrow t'}(x), \quad (3)$$

$$x = x' + f_{t' \rightarrow t}(x'). \quad (4)$$

This convention is illustrated on fig. 2. Because, in general, the driving dynamics of organelle motion are unknown, the precise form of the fields  $\{f_{t \rightarrow t'}(\cdot)\}_{t,t'}$  is unknown too. Nevertheless, as we describe next, we estimate these fields directly from the raw images in  $\mathcal{D}$ .

For our purpose (see Sect. 2.3, below), it is sufficient to compute displacement fields only at successive time levels. In particular, these are *1-level forward*  $f_{n,+}(\cdot) : \mathbb{R}^2 \mapsto \mathbb{R}^2$  and *1-level backward*  $f_{n,-}(\cdot) : \mathbb{R}^2 \mapsto \mathbb{R}^2$  fields, defined by

$$f_{n,+}(\cdot) = f_{t_n \rightarrow t_{n+1}}(\cdot), \quad n = 1, \dots, N - 1 \quad (5)$$

$$f_{n,-}(\cdot) = f_{t_n \rightarrow t_{n-1}}(\cdot), \quad n = 2, \dots, N. \quad (6)$$

We compute the displacement fields following a velocimetric approach [40, 52]. For this, we first compute displacements  $\{\{\bar{f}_{n,+}^j\}_{n=1}^{N-1}, \{\bar{f}_{n,-}^j\}_{n=2}^N\}_{j=1}^J \subset \mathbb{R}^2$  at selected positions  $\{\bar{x}^j\}_{j=1}^J \subset \mathbb{R}^2$ . In particular, given a

selected position  $\bar{x}^j$ , we compute the displacements  $\bar{f}_{n,+}^j, \bar{f}_{n,-}^j$  by standard image registration methods [54] between a sub-region of pixels, centered around  $\bar{x}^j$ , in image  $\mathcal{F}_n$  and the images  $\mathcal{F}_{n+1}, \mathcal{F}_{n-1}$ , respectively. Briefly, we consider a transformation  $T_{\delta,\theta} : \mathbb{R}^2 \mapsto \mathbb{R}^2$  that translates by  $\delta \in \mathbb{R}^2$  and rotates by an angle  $\theta \in [0, 2\pi)$ . Further, we consider  $\bar{A}^j$  gathering all pixels  $p$  such that  $\|\bar{x}^j - x^p\|_\infty \leq w_{max}$ , where  $w_{max} > 0$  is a parameter controlling the side length of the region under registration, which we set to a small multiple of the typical organelle size. Under these definitions, image registration reduces to solving the following minimization problems

$$\bar{f}_{n,+}^j = \arg \min_{\delta} \left[ \min_{\theta} \sum_{p \in \bar{A}^j} \left| I_n^p - I_{n+1}^{[T_{\delta,\theta}(x^p)]} \right|^2 \right], \quad j = 1, \dots, J, \quad n = 1, \dots, N-1 \quad (7)$$

$$\bar{f}_{n,-}^j = \arg \min_{\delta} \left[ \min_{\theta} \sum_{p \in \bar{A}^j} \left| I_n^p - I_{n-1}^{[T_{\delta,\theta}(x^p)]} \right|^2 \right], \quad j = 1, \dots, J, \quad n = 2, \dots, N \quad (8)$$

where  $[x] \in \{1, \dots, P\}$  denotes the index of the pixel closest to  $x \in \mathbb{R}^2$ . Additionally, to exclude arbitrarily large displacements, we restrict each minimization over only displacements  $\|\delta\| \leq d_{max}$ , where  $d_{max} > 0$  is an upper bound on the longest distance an organelle can travel during one exposure  $\Delta t$ .

To extend our discrete displacements over the entire  $\mathbb{R}^2$  support, and to obtain globally defined displacement fields, and to account for the errors introduced by prediction, we adopt a representation for the *forward field*

$$f_{1,+}(\cdot) = u_{1,+}(\cdot), \quad (9)$$

$$f_{n,+}(\cdot) = \Psi_+(f_{n-1,+}(\cdot)) + u_{n,+}(\cdot), \quad n = 2, \dots, N-1 \quad (10)$$

and, similarly, a representation for the *backward field*

$$f_{n,-}(\cdot) = \Psi_-(f_{n+1,-}(\cdot)) + u_{n,-}(\cdot), \quad n = 2, \dots, N-1 \quad (11)$$

$$f_{N,-}(\cdot) = u_{N,-}(\cdot), \quad (12)$$

where  $\Psi_+(\cdot) : \mathbb{R}^2 \mapsto \mathbb{R}^2$  and  $\Psi_-(\cdot) : \mathbb{R}^2 \mapsto \mathbb{R}^2$  describe how the displacement fields changes from one frame to the very next one and very previous one, respectively.  $\{u_{n,+}(\cdot)\}_{n=1}^{N-1}$  and  $\{u_{n,-}(\cdot)\}_{n=2}^N$  are independent Gaussian processes [53] with zero mean and covariance that correlates the x or the y components of the displacement fields according to a kernel  $K(\cdot, \cdot) : \mathbb{R}^2 \times \mathbb{R}^2 \mapsto (0, \infty)$ , but, to facilitate the computations leaves x and y components independent from each other, then discuss this later. To ensure smooth fields that do not change rapidly over organelles, we use the squared exponential kernel

$$K(x, x') = \sigma_u^2 \exp \left( -\frac{1}{2} \left( \frac{\|x - x'\|}{\ell} \right)^2 \right), \quad (13)$$

where  $\sigma_u^2 > 0$  is a constant and we set  $\ell > 0$  approximately equal to the diameter of a single organelle.

As we mentioned, the displacements  $\{\{\bar{f}_{n,+}^j\}_{n=1}^{N-1}, \{\bar{f}_{n,-}^j\}_{n=2}^N\}_j$  computed this way are discrete. Additionally, because image registration is imperfect, may deviate from the true displacements at the corresponding positions  $\{\{f_{n,+}(\bar{x}^j)\}_{n=1}^{N-1}, \{f_{n,-}(\bar{x}^j)\}_{n=2}^N\}_j \subset \mathbb{R}^2$ . Subsequently, to account for the errors by image registration, we finally combine these fields with the displacements  $\{\{\bar{f}_{n,+}^j\}_{n=1}^{N-1}, \{\bar{f}_{n,-}^j\}_{n=2}^N\}_j$  computed via image registration through a phenomenological observation model

$$\bar{f}_{n,+}^j = f_{n,+}(\bar{x}^j) + v_{n,+}^j, \quad n = 1, \dots, N-1 \quad (14)$$

$$\bar{f}_{n,-}^j = f_{n,-}(\bar{x}^j) + v_{n,-}^j, \quad n = 2, \dots, N \quad (15)$$

where  $\{v_{n,+}\}_{n=1}^{N-1}$  and  $\{v_{n,-}\}_{n=2}^N$  are independent uncorrelated bivariate Gaussian random variables with zero mean and variances  $\sigma_v^2 > 0$ , then discuss this later.

$$\begin{array}{ccccccc}
f_{0,+} & \rightarrow & f_{1,+} & \rightarrow & f_{2,+} & \rightarrow & f_{3,+} \rightarrow f_{4,+} \rightarrow \cdots \\
\downarrow & & \downarrow & & \downarrow & & \downarrow \\
\bar{f}_{1,+} & & \bar{f}_{2,+} & & \bar{f}_{3,+} & & \bar{f}_{4,+}
\end{array}$$

(a)

$$\begin{array}{ccccccc}
f_{N+1,-} & \rightarrow & f_{N,-} & \rightarrow & f_{N-1,-} & \rightarrow & f_{N-2,-} \rightarrow f_{N-3,-} \rightarrow \cdots \\
\downarrow & & \downarrow & & \downarrow & & \downarrow \\
\bar{f}_{N,-} & & \bar{f}_{N-1,-} & & \bar{f}_{N-2,-} & & \bar{f}_{N-3,-}
\end{array}$$

(b)

Figure 3: The relations of forward fields and backward fields are indicated here. (a) shows the approach depiction of forward displacement fields, (b) shows the approach depiction of backward displacement fields.

Eqs. (9)-(12), can be discretized in space and, combined with eqs. (14), (15), result in representations for each displacement field similar to the hidden Markov model (HMM) [2, 7, 39] resulting from the discretization of the forward field only. We employ the theory of Kalman filtering for the computation of our field estimates. Explicitly, to discretize eqs. (9)-(12), we apply a grid of fixed positions  $\{\bar{x}^\lambda\}_{\lambda=1}^\Lambda \subset \mathbb{R}^2$  that may not, in general, coincide with  $\{\bar{x}^j\}_j$ . Next, let  $\phi_{n,+}(\cdot) : \mathbb{R}^2 \mapsto \mathbb{R}$ , with  $n = 1, \dots, N-1$ , denote the x component of the displacement field  $f_{n,+}(\cdot)$ .

Denote  $\begin{bmatrix} \phi_{n,+}(\bar{x}^1) \\ \vdots \\ \phi_{n,+}(\bar{x}^\Lambda) \end{bmatrix}$  by  $\Phi_{n,+}(\bar{X}^\Lambda)$  and denote  $\begin{bmatrix} \phi_{n,+}(\bar{x}^1) \\ \vdots \\ \phi_{n,+}(\bar{x}^J) \end{bmatrix}$  by  $\Phi_{n,+}(\bar{X}^J)$ , then according to the Gaussian process  $u_{1,+}(\cdot)$ , eq. (9) becomes

$$\begin{bmatrix} \Phi_{1,+}(\bar{X}^\Lambda) \\ \Phi_{1,+}(\bar{X}^J) \end{bmatrix} \sim N_{\Lambda+J}(0_{(\Lambda+J) \times 1}, \Sigma), \quad (16)$$

$$\text{where } \Sigma = \left[ \begin{array}{ccc|ccc} K(\bar{x}^1, \bar{x}^1) & \dots & K(\bar{x}^1, \bar{x}^\Lambda) & K(\bar{x}^1, \bar{x}^1) & \dots & K(\bar{x}^1, \bar{x}^J) \\ \vdots & \ddots & \vdots & \vdots & \ddots & \vdots \\ K(\bar{x}^\Lambda, \bar{x}^1) & \dots & K(\bar{x}^\Lambda, \bar{x}^\Lambda) & K(\bar{x}^\Lambda, \bar{x}^1) & \dots & K(\bar{x}^\Lambda, \bar{x}^J) \\ \hline K(\bar{x}^1, \bar{x}^1) & \dots & K(\bar{x}^1, \bar{x}^\Lambda) & K(\bar{x}^1, \bar{x}^1) & \dots & K(\bar{x}^1, \bar{x}^J) \\ \vdots & \ddots & \vdots & \vdots & \ddots & \vdots \\ K(\bar{x}^J, \bar{x}^1) & \dots & K(\bar{x}^J, \bar{x}^\Lambda) & K(\bar{x}^J, \bar{x}^1) & \dots & K(\bar{x}^J, \bar{x}^J) \end{array} \right].$$

According to the Gaussian processes  $\{u_{n,+}(\cdot)\}_{n=2}^{N-1}$ , eqs. (10) become

$$\begin{bmatrix} \Phi_{n,+}(\bar{X}^\Lambda) \\ \Phi_{n,+}(\bar{X}^J) \end{bmatrix} \sim N_{\Lambda+J}\left(\Psi_+\left(\begin{bmatrix} \Phi_{n-1,+}(\bar{X}^\Lambda) \\ \Phi_{n-1,+}(\bar{X}^J) \end{bmatrix}\right), \Sigma\right), \quad (17)$$

where  $n = 2, \dots, N-1$ .

Similarly, let  $\bar{\phi}_{n,+}^j \in \mathbb{R}$  denote the x component of  $\bar{f}_{n,+}^j$  and further denote the vector  $\begin{bmatrix} \bar{\phi}_{n,+}^1 \\ \vdots \\ \bar{\phi}_{n,+}^J \end{bmatrix}$  by  $\bar{\Phi}_{n,+}^J$ . Then eq. (14) become

$$\bar{\Phi}_{n,+}^J \sim N_J \left( \begin{bmatrix} 0_{J \times \Lambda} & I_{J \times J} \end{bmatrix} \begin{bmatrix} \Phi_{n,+}(\bar{X}^\Lambda) \\ \Phi_{n,+}(\bar{X}^J) \end{bmatrix}, \sigma_v^2 I \right), \quad n = 1, \dots, N-1. \quad (18)$$

Similar formulas apply for the y-component  $\psi_{n,+}(\cdot) : \mathbb{R}^2 \mapsto \mathbb{R}$  of the forward field, as well as for the x-component  $\phi_{n,-}(\cdot) : \mathbb{R}^2 \mapsto \mathbb{R}$  and y-component  $\psi_{n,-}(\cdot) : \mathbb{R}^2 \mapsto \mathbb{R}$  of the backward field. We provide the complete set of equations in the SUPPORTING INFORMATION.

Let notation  $[.]^j$  to denote the vector, which contains all elements depending on possible value  $j$ . In eqs. (16)(17),  $\{[\phi_{n,+}^j]\}_{n=1}^{N-1}$  are the states in space  $\mathbb{R}^{\Lambda+J}$ , in which predictions are made based on  $\Psi_+(\cdot)$ (see eqs. (10)(17)), and  $\{[\bar{\phi}_{n,+}^j]\}_{n=1}^{N-1}$  are the states in space  $\mathbb{R}^J$ , in which the observations are obtained by applying image registration to the image data.  $\Psi_+(\cdot)$  is a prediction function, which gives a prediction in the very next level when a forward field is given, it could be a diffusion equation of a dynamic system if it was known or just a simple guess based on our previous experience.  $\{[u_{n,+}^j]\}_{n=1}^{N-1}$  are the prediction noises, each follows a multiple Gaussian distribution with mean 0 and kernel covariance matrix  $\Sigma$  in eq. (16), with the definition of Gaussian process kernel in eq. (13),  $\sigma_u$  presents the credibility of prediction system, that is, if  $\Psi(\cdot)$  is quite believable then  $\sigma_u$  should choose to be small, vice versa, if  $\Psi(\cdot)$  is just a rough guess then  $\sigma_u$  should be relatively large;  $\{[v_{n,+}^j]\}_{n=1}^{N-1}$  are the observation noises, each follows a multiple Gaussian distribution with mean 0 and a co-variance matrix  $\sigma_v^2 I$ , where  $I$  is a  $J$  by  $J$  identity matrix,  $\sigma_v$  in eq. (18) measures the reliability of observation, a more precise method to acquire  $\{\bar{f}_{n,+}^j\}_{n=1}^{N-1}$  will lead to smaller  $\sigma_v$ . There is a special case when  $\Psi(\cdot)$  is an identity function, it happens when one trust the displacement fields reserve the same status as the previous level.

From the equations (9)(10)(14) and their vectorized discrete form (16)(17)(18) for forward fields, a sequence of improved estimations  $\{\hat{\phi}_{n,+}^j\}_{n=1}^{N-1}$  can be obtained by applying Kalman filtering(KF). However, Kalman filtering only works with linear Gaussian system,  $\Psi_+(\cdot)$  must be linear, i.e., eq. (10) only take the form as  $[\phi_{n+1,+}^j] = A[\phi_{n,+}^j] + [u_{n+1,+}^j]$ , where  $A$  is a  $(\Lambda + J)$  by  $(\Lambda + J)$  matrix. Because of this limitation, a more robust and universal method is needed for both linear and nonlinear systems. We address this problem by incorporating Ensemble Kalman Filtering(EnKF)[26] for organelles trajectories prediction. EnKF for our problem is summarized in Algorithm 1.

In the algorithm 1,  $E$  is the size of an ensemble set we choose. Instead of using a single one estimation, EnKF generates an ensemble of samples  $\hat{\phi}_{n+1}^{(e)}$  as multiple predictions in eq. (19), where one sample is corresponding to one simulation satisfying eq. (17), therefore, it is applicable to either linear or nonlinear system, sample mean and sample variance in the following updating steps are computed by this ensemble set as eq. (20) and eq. (21). Also, the improved approximation  $[\hat{\phi}_{n+1,+}^j]$  is a weighted sum of predictions  $\hat{\phi}_{n+1}^{(e)}$  and observation  $[\bar{\phi}_{n+1,+}^j]$  based on prediction noise and observation noise,  $G_{n+1}$  of eq. (22) is the Kalman gain, which determs the weight between the prediction noise and observation noise. If the observation is more reliable or  $\sigma_v$  is much smaller,  $\lim_{R \rightarrow 0} K_{n+1} = I$ , it will make  $I - K_{n+1}$  close to 0, then  $\hat{\phi}_{n+1}^{(e)}$  in eq. (23) has less information from the mean of predictions  $\hat{m}_{n+1}$ , but contains more information from the observation  $[\bar{\phi}_{n+1,+}^j]$ , thus the observation will have more weight in the final improved estimation. Conversely, if the prediction process is more trustworthy, or equivalently,  $\sigma_u$  is smaller, the improved estimation weights the predictions more heavily[3].

The y component of forward fields and backward fields filtering process works in a similar way. With the discretized equations given in SUPPORTING INFORMATION and the approach depiction in figure 3, one could perform the EnKF to obtained the improved estimations  $\{\hat{\psi}_{n,+}^j\}_{n=1}^N$ ,  $\{\hat{\phi}_{n,-}^j\}_{n=1}^N$  and  $\{\hat{\psi}_{n,-}^j\}_{n=1}^N$ .

---

**Algorithm 1. Ensemble Kalman Filter**

When  $n = 0$ ,

$$\phi_0^{(e)} = 0, \quad e = 1, \dots, E$$

$$Q = \Sigma$$

$$R = \sigma_v^2 I$$

$$\hat{\phi}_1^{(e)} = \phi_0^{(e)} + Q_0^{(e)}, \quad Q_0^{(e)} \sim N(0, Q), \quad e = 1, \dots, E$$

$$\hat{m}_1 = \frac{1}{E} \sum_{e=1}^E \hat{\phi}_1^{(e)}$$

$$\hat{C}_1 = \frac{1}{E-1} \sum_{e=1}^E (\hat{\phi}_1^{(e)} - \hat{m}_1)(\hat{\phi}_1^{(e)} - \hat{m}_1)^T$$

$$G_1 = \hat{C}_1(\hat{C}_1 + R)^{-1}$$

$$[\hat{\phi}_{1,+}^j] = (I - G_1)\hat{m}_1 + G_1[\bar{\phi}_{1,+}^j]$$

$$\phi_1^{(e)} = [\hat{\phi}_{1,+}^j] + R_1^{(e)}, \quad R_1^{(e)} \sim N(0, R), \quad e = 1, \dots, E$$

For  $n = 1$  to  $N - 2$

$$\hat{\phi}_{n+1}^{(e)} = \Psi_+(\phi_n^{(e)}) + Q_n^{(e)}, \quad Q_n^{(e)} \sim N(0, Q), \quad e = 1, \dots, E \quad (19)$$

$$\hat{m}_{n+1} = \frac{1}{E} \sum_{e=1}^E \hat{\phi}_{n+1}^{(e)} \quad (20)$$

$$\hat{C}_{n+1} = \frac{1}{E-1} \sum_{e=1}^E (\hat{\phi}_{n+1}^{(e)} - \hat{m}_{n+1})(\hat{\phi}_{n+1}^{(e)} - \hat{m}_{n+1})^T \quad (21)$$

$$G_{n+1} = \hat{C}_{n+1}(\hat{C}_{n+1} + R)^{-1} \quad (22)$$

$$[\hat{\phi}_{n+1,+}^j] = (I - G_{n+1})\hat{m}_{n+1} + G_{n+1}[\bar{\phi}_{n+1,+}^j] \quad (23)$$

$$\phi_{n+1}^{(e)} = [\hat{\phi}_{n+1,+}^j] + R_{n+1}^{(e)}, \quad R_{n+1}^{(e)} \sim N(0, R), \quad e = 1, \dots, E \quad (24)$$


---

### 2.3 Topological reconstruction

Given a collection of organelle space-time localizations  $\tilde{\mathcal{R}}$  and appropriate displacement fields  $\{f_{n,+}(\cdot)\}_{n=1}^{N-1}$  and  $\{f_{n,-}(\cdot)\}_{n=2}^N$ , our goal is the computational reconstruction of  $\{r_a\}_a$ . Of course, because the reconstruction of  $\{r_a\}_a$  in continuous time is impossible without a motion model that can interpolate over time, which for plant organelles is unavailable, we focus on reconstructing the trajectories  $\{\tilde{r}_a\}_a$  that are discretized at the time levels contained in  $\tilde{\mathcal{R}}$ , i.e.  $\tilde{r}_a = \{r_a(t_n)\}_n$ . As we show below, for such discrete reconstruction the computed displacement fields  $\{f_{n,+}(\cdot)\}_{n=1}^{N-1}$  and  $\{f_{n,-}(\cdot)\}_{n=2}^N$  are sufficient.

We adopt a similar linking process as in [42]. Our algorithm (described in depth below) proceeds in three stages, it has been exhibited in fig. 4. In the *first stage*, we embed  $\tilde{\mathcal{R}}$  into

$$\mathcal{R} = \bigcup_a \{(r_a(t), t)\}_{t \in [0, T]} \subset \mathbb{R}^2 \times [0, T]. \quad (25)$$

For any two points  $(x, t) \in \mathbb{R}^2 \times [0, T]$  and  $(x', t') \in \mathbb{R}^2 \times [0, T]$ , we consider

$$d((x, t), (x', t')) = \|x - x'\| + \alpha|t - t'| \quad (26)$$

where  $\|\cdot\|$  is the Euclidean norm in  $\mathbb{R}^2$  and  $\alpha > 0$  is a constant. Since  $d$  is a distance in  $\mathbb{R}^2 \times [0, T]$ , our main object of interest  $\mathcal{R} \subset \mathbb{R}^2 \times [0, T]$  inherits the topological properties of a metric space [14, 34, 48]. Essentially,  $\mathcal{R}$  consists of the points in space-time  $\mathbb{R}^2 \times [0, T]$  that are visited by the organelles during the course of the experiment. Although  $\mathcal{R}$  captures globally the motion we are interested in revealing, it leaves individual trajectories indistinguishable. Accordingly, in the *second stage*, we partition the set  $\mathcal{R}$  into components  $\{\mathcal{R}_a\}_a$  such that each  $\mathcal{R}_a$  corresponds to a single trajectory  $r_a$ , i.e. we partition  $\mathcal{R} = \cup_a \mathcal{R}_a$  such that  $\mathcal{R}_a = \{(r_a(t), t)\}_{t \in [0, T]} \subset \mathbb{R}^2 \times [0, T]$ . The partitioning of  $\mathcal{R}$  can be achieved computationally through the construction of an appropriate topological nerve [13] according to the *Mapper algorithm* [8, 44]. Briefly, for any  $\tau > 0$ , such that  $\tau < \Delta t$ , we consider the overlapping intervals  $\{\mathcal{T}_n\}_{n=1}^{N-1}$  defined by

$$\mathcal{T}_1 = [t_1, t_2 + \tau) \quad (27)$$

$$\mathcal{T}_n = (t_n - \tau, t_{n+1} + \tau), \quad n = 2, \dots, N - 2 \quad (28)$$

$$\mathcal{T}_{N-1} = (t_{N-1} - \tau, t_N] \quad (29)$$

that are associated with the time levels  $\{t_n\}_n$  of the provided dataset. Further, for any  $(x, t) \in \mathcal{R}$  we consider the temporal projection  $P_{\mathcal{R}} : \mathcal{R} \mapsto [0, T]$  defined by

$$P_{\mathcal{R}}((x, t)) = t, \quad (x, t) \in \mathcal{R} \quad (30)$$

Due to continuity,  $\{P_{\mathcal{R}}^{-1}(\mathcal{T}_n)\}_{n=1}^{N-1} \subset \mathcal{R}$  forms an open covering of  $\mathcal{R}$ . By its definition, each pre-image  $P_{\mathcal{R}}^{-1}(\mathcal{T}_n) \subset \mathcal{R}$  contains segments of at least one organelle trajectory; nevertheless, because of the inherited topology, each trajectory segment corresponds to only a single connected component within  $P_{\mathcal{R}}^{-1}(\mathcal{T}_n) \subset \mathcal{R}$ . Consequently, partitioning  $\mathcal{R}$  into connected components is achieved by, first, partitioning each  $P_{\mathcal{R}}^{-1}(\mathcal{T}_n)$  into its connected components  $\{\mathcal{S}_{m,n}\}_{m=1}^{M_n}$  and, subsequently, computing the nerve of the entire resulting family of components  $\{\{\mathcal{S}_{m,n}\}_{m=1}^{M_n}\}_{n=1}^{N-1} \subset \mathcal{R}$ , which is also an open covering of  $\mathcal{R}$ . Finally, in the *third stage*, we readily obtain discrete trajectories  $\tilde{r}_a$  by the intersections  $\mathcal{R}_a \cap \tilde{\mathcal{R}}$ . To partition each  $P_{\mathcal{R}}^{-1}(\mathcal{T}_n)$  into its connected components  $\{\mathcal{S}_{m,n}\}_m$ , we consider

$$\ell((x, t), (x', t')) = \|x - x' - f_{t' \rightarrow t}(x')\| + \|x' - x - f_{t \rightarrow t'}(x)\| \quad (31)$$

where  $(x, t) \in \mathbb{R}^2 \times [0, T]$  and  $(x', t') \in \mathbb{R}^2 \times [0, T]$ .  $(x, t) \in P_{\mathcal{R}}^{-1}(\mathcal{T}_n)$  and  $(x', t') \in P_{\mathcal{R}}^{-1}(\mathcal{T}_n)$ , belong in the same connected component  $S_{m,n}$  if and only if  $\ell((x, t), (x', t')) = 0$ . Therefore, provided the 1-level displacement fields  $\{f_{n,+}(\cdot)\}_{n=1}^{N-1}$  and  $\{f_{n,-}(\cdot)\}_{n=2}^N$  have been already computed, we can use  $\ell$  to topologically characterize trajectory segments or equivalently connected components of  $P_{\mathcal{R}}^{-1}(\mathcal{T}_n)$ . Consequently, a computational

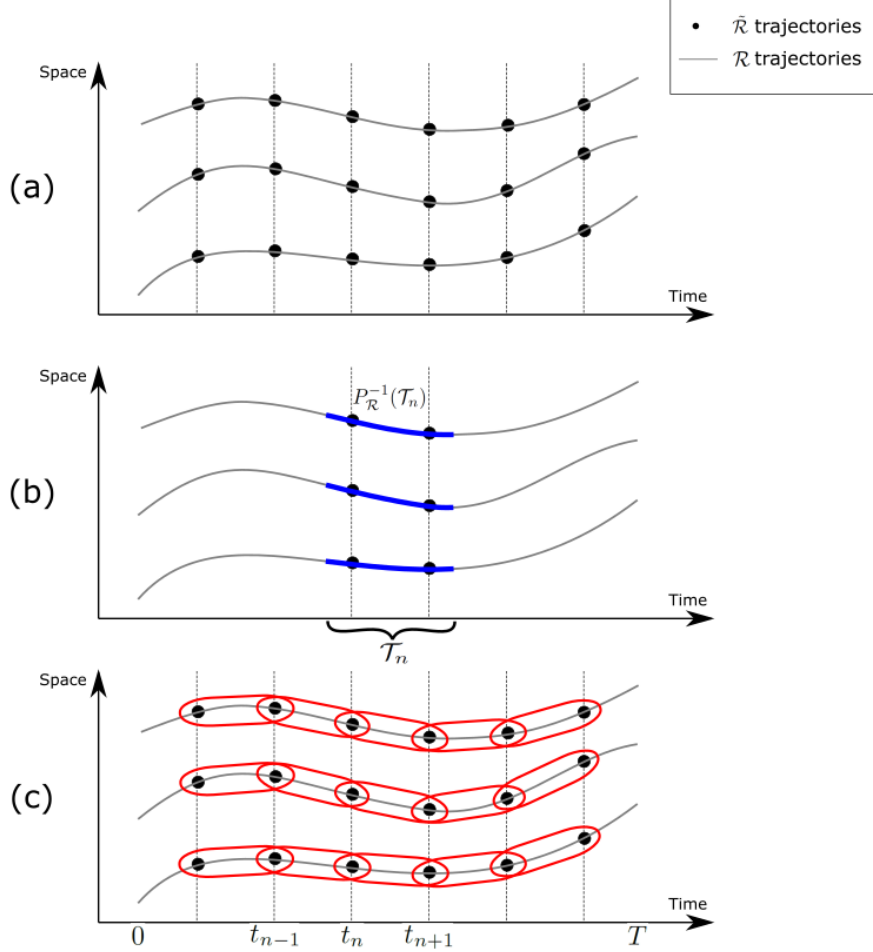


Figure 4: (a) shows  $\tilde{\mathcal{R}}$  and  $\mathcal{R}$  with lines; (b) shows  $\mathcal{R}$ ,  $\mathcal{T}_n$  and  $P_{\mathcal{R}}^{-1}(\mathcal{T}_n)$  as blue segments; (c) shows  $\mathcal{R}$ ,  $\mathcal{T}_n$ ,  $P_{\mathcal{R}}^{-1}(\mathcal{T}_n)$ ,  $\tilde{\mathcal{R}}$  and reconstructed discrete trajectories.

characterization of  $\tilde{\mathcal{S}}_{m,n} = \mathcal{S}_{m,n} \cap \tilde{\mathcal{R}}$  can be achieved by an agglomerative clustering on  $P_{\mathcal{R}}^{-1}(\mathcal{T}_n) \cap \tilde{\mathcal{R}}$  with linkage  $\ell$ . Specifically, the restriction  $\ell_n$  of  $\ell$  in  $P_{\mathcal{R}}^{-1}(\mathcal{T}_n) \cap \tilde{\mathcal{R}}$ , required for each clustering, reduces to

$$\ell_n((x, t), (x', t')) = \begin{cases} \|x - x' - f_{n+1,-}(x')\| + \|x' - x - f_{n,+}(x)\|, & t < t' \\ 2\|x - x'\|, & t = t' \\ \|x - x' - f_{n,+}(x')\| + \|x' - x - f_{n+1,-}(x)\|, & t > t' \end{cases}. \quad (32)$$

### 3 Results

This method has been applied to two simulated videos and one real video. The results and analysis are shown in the following subsections.

### 3.1 Velocimetry benchmark

The displacement estimation process and linking process are tested on a simulated data set consisting of 20 organelles in totally 100 frames with time delay  $\Delta t = 1\text{s}$ . The trajectories are exhibited in figure 5. The positions of an organelle in each frame are known and are generated by a diffusion process, which contains both diffusion term and drift term, as follows

$$dX_t = 3dt + dW_t, \quad (33)$$

$$dY_t = dt + dW_t, \quad (34)$$

where  $W_t$  is a Wiener process. The starting distances between any two adjacent organelles at  $t = 0\text{s}$  is 10 pixels.

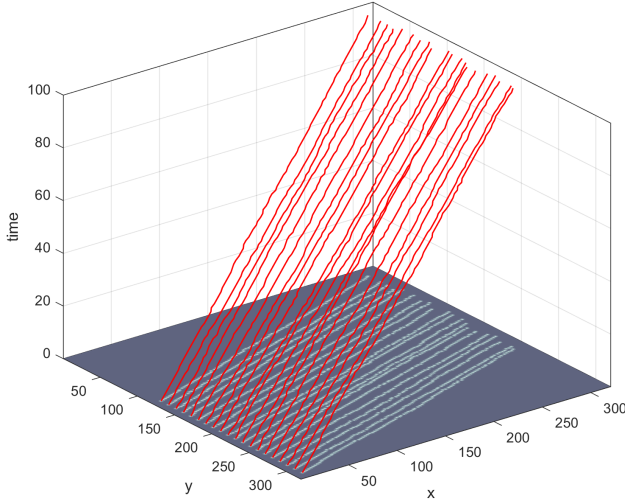


Figure 5: The frame size is 320 by 320 pixels. Trajectories of 20 organelles are in red spanning from time  $t = 0\text{s}$  to  $t = 99\text{s}$ , their motion is caught by a diffusion process containing both a diffusion term and a drift term. The starting distance of any two adjacent organelles at  $t = 0\text{s}$  is 10 pixels.

Given the location of all organelles in each frame, apply our displacement estimation process in Section 2.2 to the data set, then calculate the mean error(in pixels) between the estimated forward (backward) displacement and true displacement frame by frame, along x-axis and y-axis respectively. The results are shown in figure 6. From the four histograms, almost all mean errors of one frame is around 0.25 pixel and smaller than one pixel, only very few is greater than one pixel but smaller than two pixels.

Given the displacements, we apply the linking process in Section 2.3, whose results are shown in figure 7. All organelles are correctly connected by 20 trajectories, each trajectory spans exactly from  $t = 0$  to  $t = 99$ , yielding accuracy rate is 100%.

Let's add perturbation along y-axis direction to the location of simulated organelles, i.e. adding noise, which follows a uniform distribution  $U(-\epsilon, \epsilon)$ , to the y-coordinates of every organelles at every time level. Reapply the displacement estimation process and linking process, then count number of total trajectories, number of trajectories exist at least in 10 consecutive frames, number of trajectories have 100% coincidence with the truth, number of trajectories have at least 90% coincidence with the truth and number of trajectories have at least 50% coincidence with the truth, from our algorithm. The results are in table 1,

When  $\epsilon$  goes larger, the trajectories will contain more fluctuation, on the other hand, any two adjacent trajectories will become more closer or even intersected. Thus, larger  $\epsilon$  will cause higher difficulty to detect trajectories. From the table above, when noise is mild, our reconstructed trajectories remain the same; but

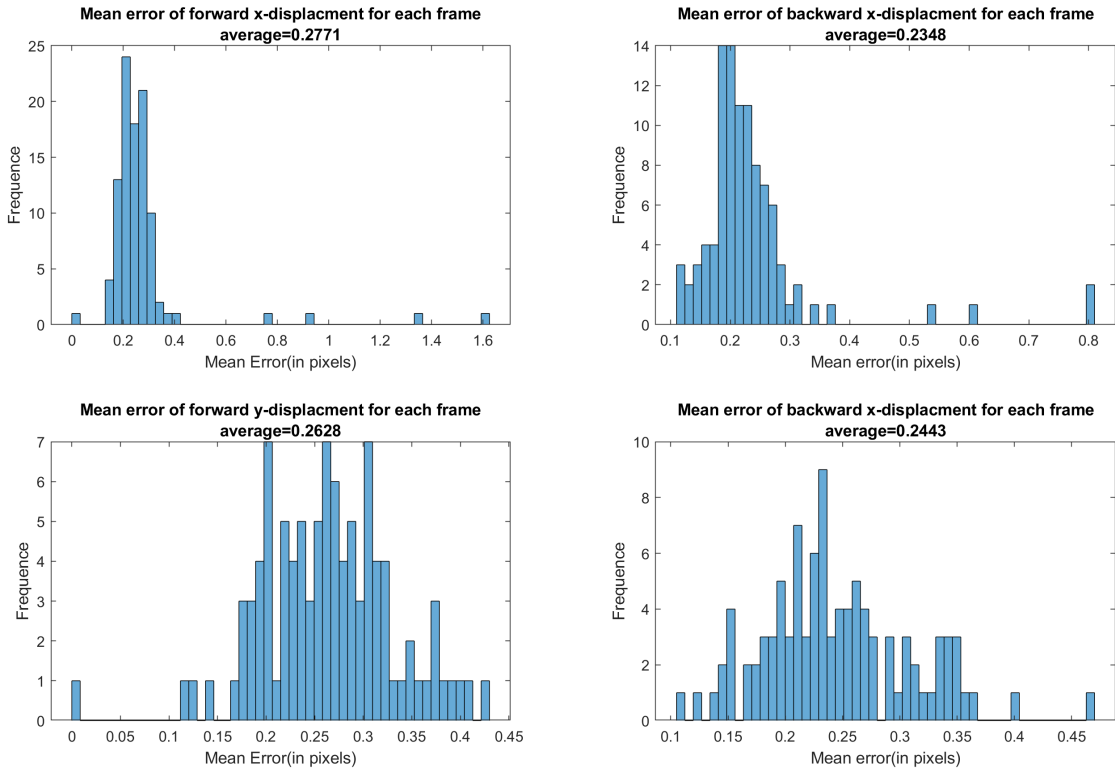


Figure 6: Four histograms of mean error of each frame. Each one compares estimated forward and backward displacement with ground truth along x-axis and y-axis, respectively.

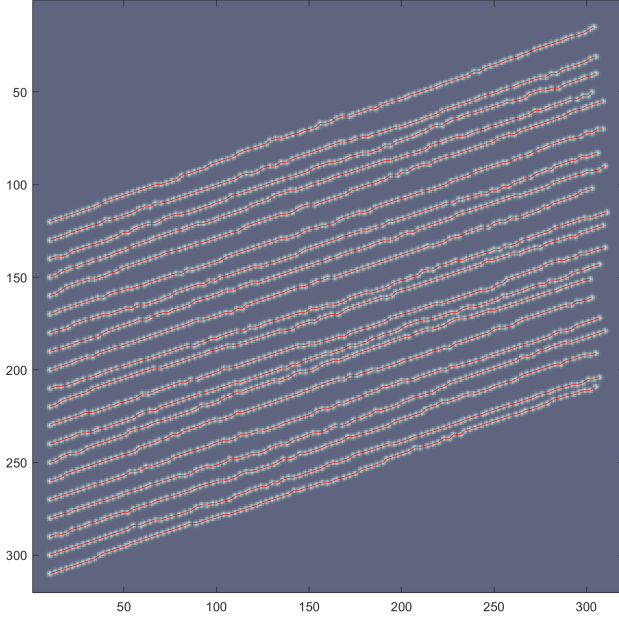


Figure 7: Linking result of all trajectories in red. The accuracy rate is 100%

$\epsilon$	total	$\geq 10F$	$= 100\%$	$\geq 90\%$	$\geq 50\%$
$\epsilon = 1$	20	20	20	20	20
$\epsilon = 1.5$	20	20	20	20	20
$\epsilon = 2$	20	20	20	20	20
$\epsilon = 2.5$	24	24	14	17	20
$\epsilon = 3$	32	27	9	14	17
$\epsilon = 3.5$	33	30	5	10	15
$\epsilon = 4$	53	40	1	4	14

Table 1: Table of detection result

when  $\epsilon$  become large, the accuracy rate decreases, actually, when  $\epsilon = 4$  pixels, there are no clear patterns for each trajectories to be detected, and all organelles just look scattered in the frame when we overlap all their positions over the time span of the whole video.

### 3.2 Complex dynamics

Now consider a complex video with 20 organelles in each frame and 100 frames in total. Each frame has a 380 by 380 pixels grid on it. This video has the frame rate as 30 frames per second, which gives  $\Delta t = 33.33$  ms. There are multiple filaments hiding in the background, which are not visible. Three kinds of motion could happen. An organelle could attach to or detach from a filament, or travels along a filament, or move randomly. Moreover, an organelle could go though these three motions in a  $\Delta t$ .

After importing the video as gray scaled images and filtering out the background from each frame, our method detects pick peaks iteratively and applies Bayesian identification with following prior distributions,

- $\hat{n}_n^p$  follows normal distribution  $N(0, 1)$ ,
- $z_n^s$  follows uniform distribution over the frame,
- $h_n^s$  follows translated beta distribution with support  $(50, 150)$ , mode 100, and shape parameter  $\alpha = 5$ ,
- $w_n^s$  follows translated beta distribution with support  $(10, 20)$ , mode 15, and shape parameter  $\alpha = 5$ ,

as we mentioned in Section 2.1. An example of frame  $t_n = 38$  is shown in figure 8. The red dots in the left sub-figure and blue pentagons in the right sub-figure are the original locations before Bayesian identification, it is obvious to see that the three pairs at the bottom(which have y-value greater than 300) need to be corrected as part of their corresponding organelles are overlapped. The red pentagons are the fitted location after Bayesian identification.

For the approximation of displacement fields using Ensemble Kalman filtering, since our  $\Delta t = 0.033$  s is extremely small, this ensures the displacement fields do not change rapidly from one frame to the very next, and the displacement fields from one level partial memorize the trend from the previous level, thus, without more information about the dynamic system, choose  $\Psi(x) = x$ . Set  $\sigma_u = 5, \sigma_v = 2$  since we want to trust observations more, then the forward displacement fields of frame  $t_n = 17$  is displayed in figure 9, an area of pixels [140, 230] on x-axis times pixels [260, 350] on y-axis is enlarged in figure 10. We can easily observe the displacement fields around organelles.

The trajectories are reconstructed in figure 11. The left sub-figure shows all estimated trajectories in red concentrate upon the light area. The right shows trajectories with ground true trajectories in black, most of them are coincide, except the area where more than two organelles are overlapped. Specifically, we pick four sets of trajectory reconstructions, exhibiting in figure 12, each sub-figure shows our reconstructions versus one true trajectory, their mean error are 1.2054, 2.2474, 2.0942 and 1.4271 in number of pixels, respectively.

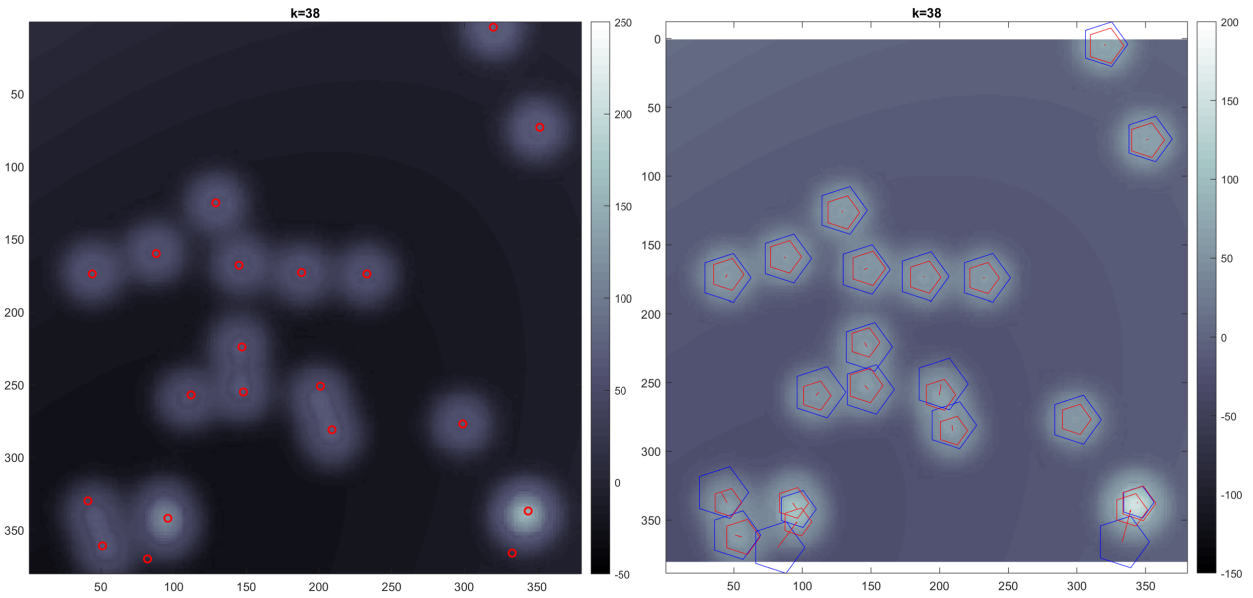


Figure 8: The left shows the rough detection result, the right show the locations after correction

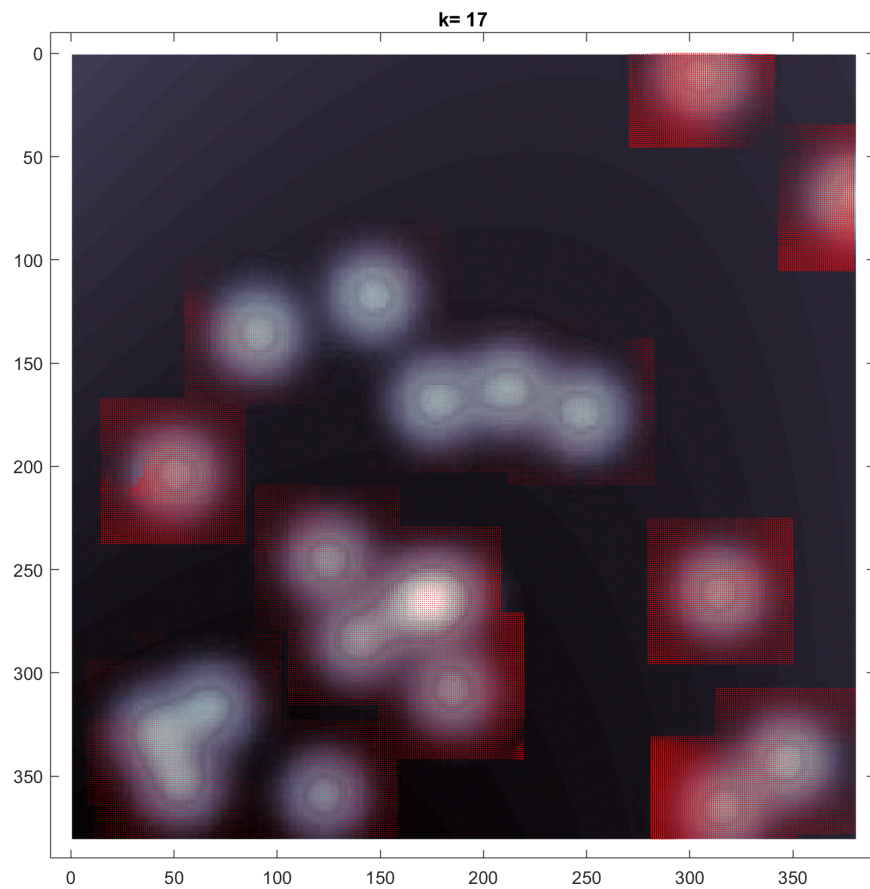


Figure 9: estimated displacement field using EnKF

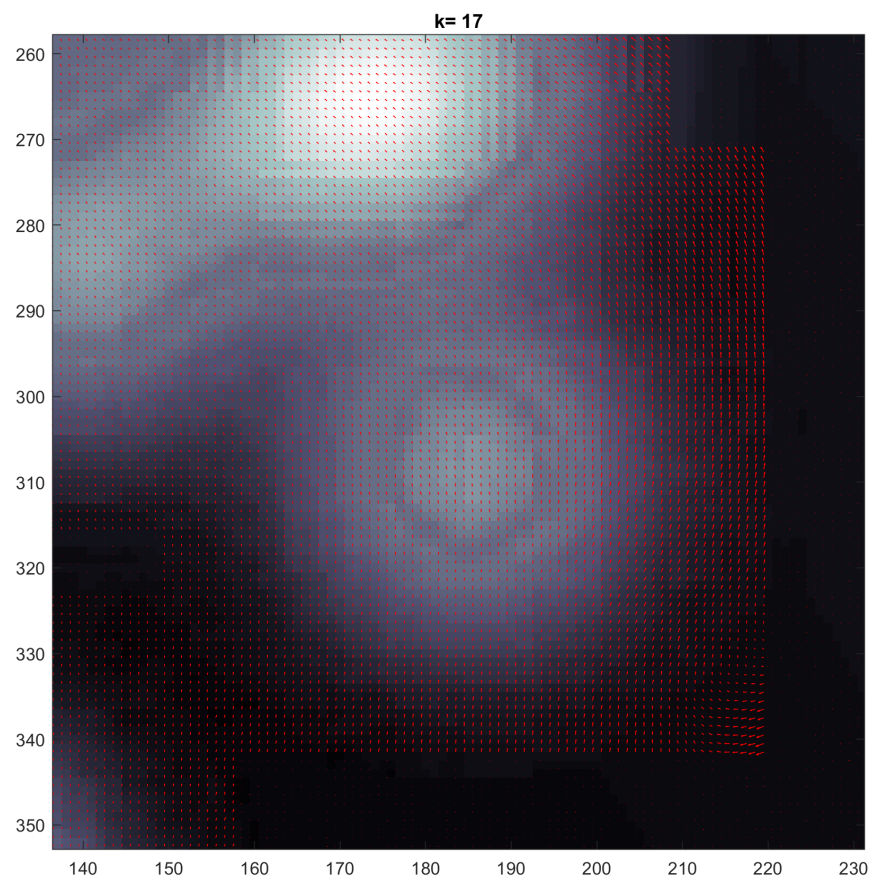


Figure 10: Amplify partial displacement field

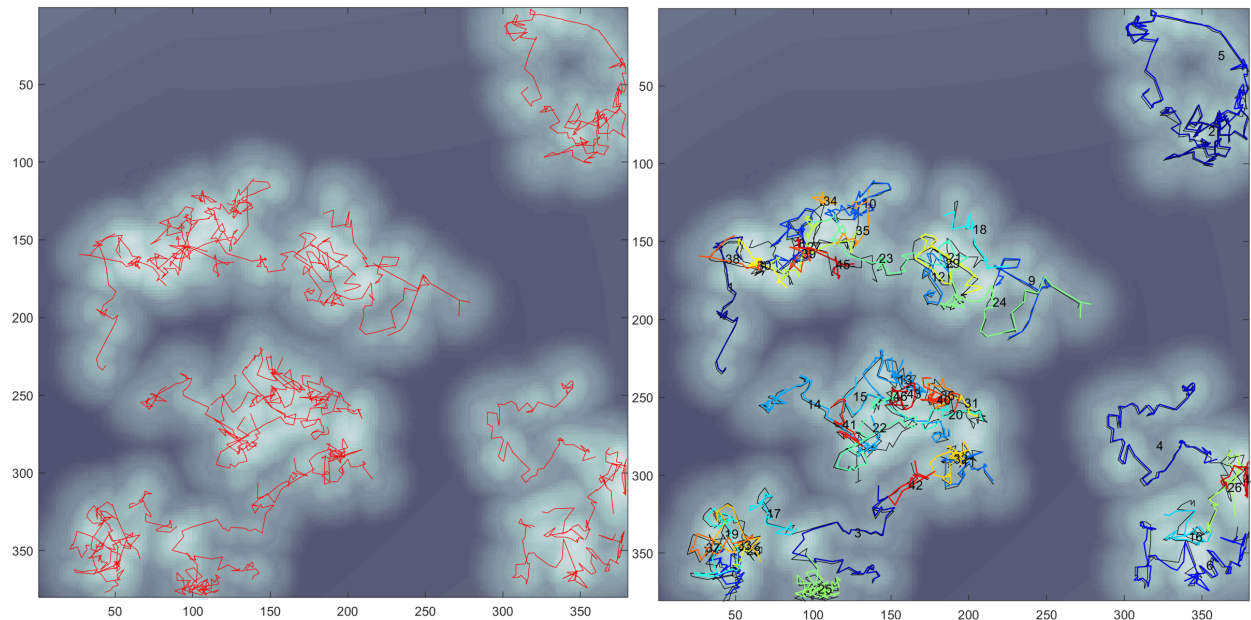


Figure 11: Trajectories reconstruction result

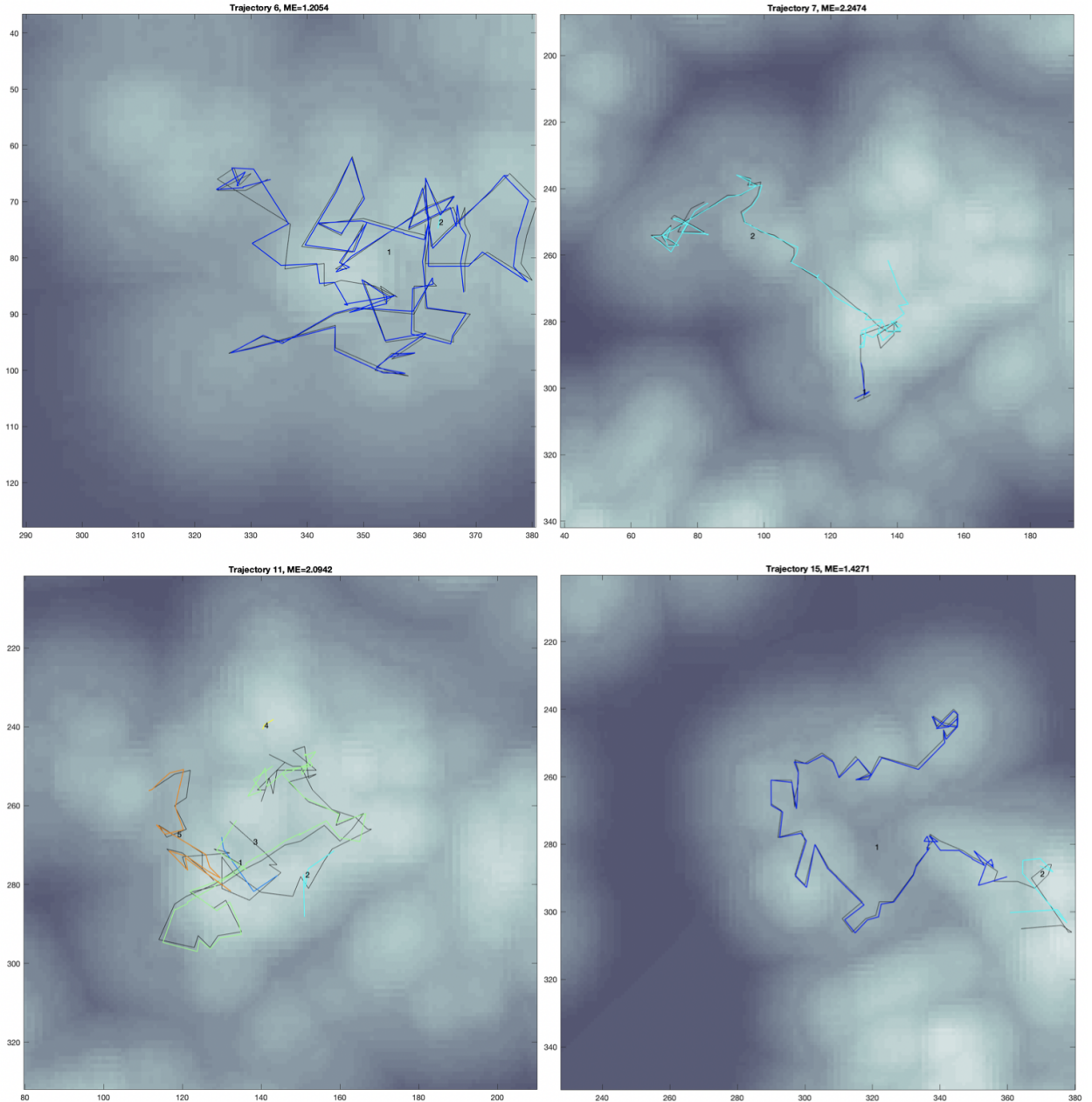


Figure 12: Four specific sets of trajectory reconstructions vs ground truth. Each sub-figure shows reconstructions versus one true trajectory. The upper left is amplified from the area  $[290, 380] \times [40, 130]$  in fig. 11; the upper right is amplified from the area  $[40, 190] \times [190, 340]$  in fig. 11; the bottom left is amplified from the area  $[80, 210] \times [200, 330]$  in fig. 11; the bottom right is amplified from the area  $[230, 380] \times [200, 350]$  in fig. 11;

### 3.3 real data dynamics

Finally, let's consider a real grayscale video with total 299 frames, capturing peroxisomes in a plant cell. The resolution (pixel size) for this video is 0.196 micrometer/pixel and the size of each frame is 79 pixels by 662 pixels. The time delay of the video is 82 ms, that is,  $\Delta t = 82$  ms. As shown in figure 13(a), it is the first frame of the video, these light spots are peroxisomes and their size is from 0.5 to 1 micrometer.

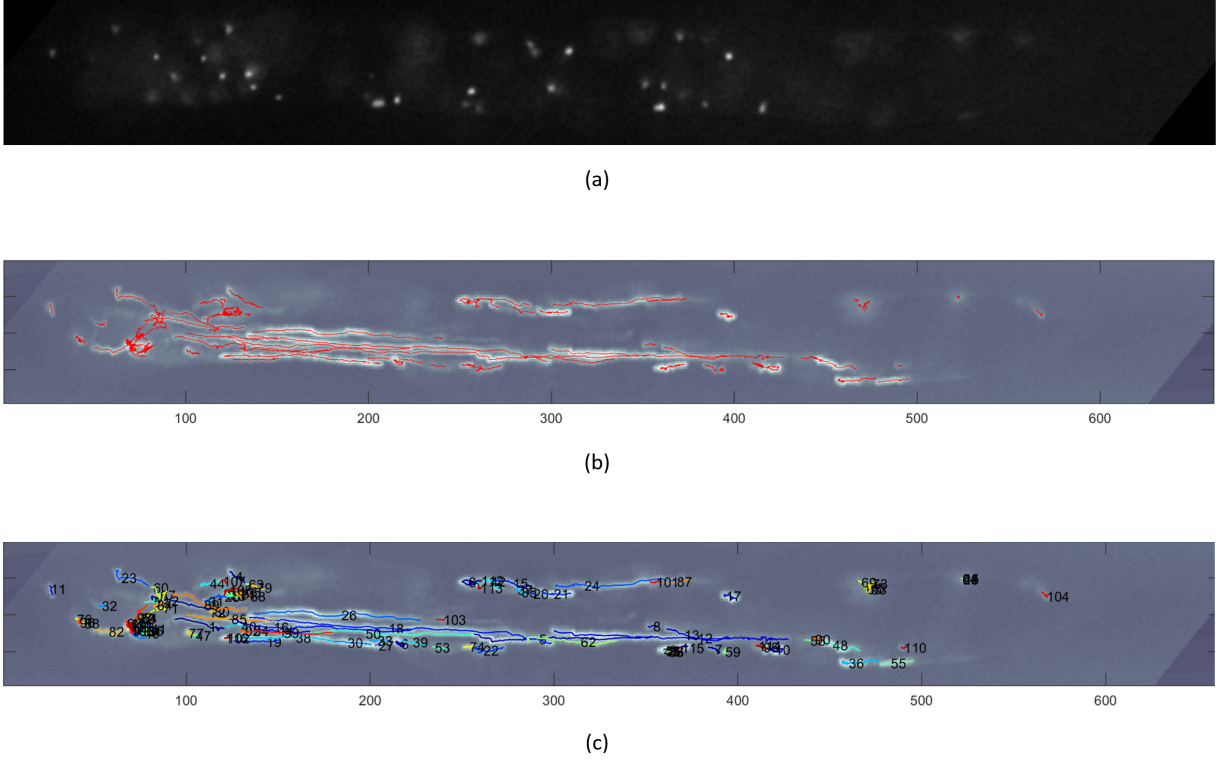


Figure 13: Figure (a) is the first frame of the video. Figure (b) exhibits all estimated trajectories in red. Figure (c) further labels each estimated trajectory in different number with variable color.

By applying our methodology to this video, the results are shown in figure 13(b) and 13(c). We plot the estimated trajectories, which only exist in at least 10 consecutive frames, in figure 13(b). As we can see that the red trajectories covers almost every highlight background area. In figure 13(c), we exhibit all these 116 trajectories in different colors with number labels. Note that our developed method is able to track the peroxisomes in different types of motions for long time intervals. Thus, mainly two type of trajectories are observed: a long trail when peroxisome is traveling along the filament; a short trail when peroxisome is wiggling in the cell.

## 4 Discussion and Conclusion

In this paper, we have developed a novel, data-oriented, method for the analysis of experimental measurements. Our method combines TDA and advanced filtering techniques. Key features of our approach include the adoption of Mapper with the necessary modifications, the use of Gaussian processes and EnKF in the steps that facilitate the clustering involved in the computation of the associated nerve.

Unlike earlier tracking approaches, our method could proceed with or without invoking a motion model. Without invoking a motion model, a simple reasonable guess can relax a strong requirement in the analysis of biological data, especially those obtained from *in vivo* microscopy; with a motion model, a more precise suggestion could be involved in the final estimation. In both cases, we estimated the displacement field from the data. Effectively, our approach resembles data-driven clustering; however, implicitly our method assumes a phenomenological motion type that is exclusively informed by the observations. In any case, reconstructed tracks are valid as long as the computation of estimated displacement fields are faithful.

Comparing to [42], EnKF works with the case with minimal assumptions, moreover, it could achieve more precise results if more knowledge of dynamic system is involved. In EnKF, it has the advantage that it can inherit some trend from last status, and it also fits the nonlinear system, which could be more widely used when a sophisticated motion model is given in the real world.

Earlier attempts obtain estimates of the displacement field using a combination of heuristics and conventional KF. Given that motion patterns are highly non-linear, conventional KF lacks robustness and no longer works. Here, instead we develop a principled approach that models the displacement fields through Gaussian processes and we apply EnKF, which can successfully estimate the correct dynamics under a wide range of motion conditions.

Despite the key innovations introduced here, our method still proceeds by breaking down the tracking problem into separate phases (i.e. identification, localization, linking, etc) similar to the conventional tracking paradigm. Although we achieve some coupling between these phases in the velocimetry stage, full coupling between them in a manner that allows improved inference in any of the phases to fuse into the other phases remains to be developed. As of that, future work is required to yield a comprehensive framework where identification, linking and velocimetry are unified and treated simultaneously. Due to high stochasticity in the underlying physics (motion, uncertainty, detection noise, etc) it is natural to seek such a monolithic approach within the Bayesian context; however, a fully Bayesian approach requires to overcome at least two important barriers: (1) Bayesian foundations of nerves and displacement fields; and (2) excessive computational cost which is expected to increase significantly.

In conclusion, we have proposed a novel algorithm to track organelles in microscopy video, which can automatically reconstruct the trajectories. This method can optimize the parameters of organelles based on images, combine your predictions with observations in estimating organelle movement, and link organelles based on topological analysis. However, it cannot do the tracking job perfectly in the case when more organelles collide or stick together. We are planning to refine it by using more accuracy method to detect the peaks and apply more fancy filtering process to improve the tracking result.

## References

- [1] Paul Bendich, Sang Peter Chin, Jesse Clark, Jonathan Desena, John Harer, Elizabeth Munch, Andrew Newman, David Porter, David Rouse, Nate Strawn, et al. Topological and statistical behavior classifiers for tracking applications. *IEEE Transactions on Aerospace and Electronic Systems*, 52(6):2644–2661, 2016.
- [2] Christopher M Bishop. *Pattern recognition and machine learning*. Springer, 2006.
- [3] G Bishop. An introduction to the kalman filter. Technical report, TR 95-041, Department of Computer Science, University of North Carolina at Chapel Hill, Chapel Hill, NC 27599-3175, Monday, 2006.
- [4] Samuel S Blackman. Multiple-target tracking with radar applications. *Dedham, MA, Artech House, Inc., 1986, 463 p.*, 1986.
- [5] Serena S v Braun and Enrico Schleiff. Movement of endosymbiotic organelles. *Current Protein and Peptide Science*, 8(5):426–438, 2007.
- [6] Giampiero Cai, Luigi Parrotta, and Mauro Cresti. Organelle trafficking, the cytoskeleton, and pollen tube growth. *Journal of integrative plant biology*, 57(1):63–78, 2015.
- [7] Olivier Cappé, Eric Moulines, and Tobias Rydén. Inference in hidden markov models. In *Proceedings of EUSFLAT conference*, pages 14–16, 2009.
- [8] Gunnar Carlsson. Topology and data. *Bulletin of the American Mathematical Society*, 46(2):255–308, 2009.
- [9] George Casella and Roger L Berger. *Statistical inference*, volume 2. Duxbury Pacific Grove, CA, 2002.
- [10] David A Collings, John DI Harper, Jan Marc, Robyn L Overall, and Robert T Mullen. Life in the fast lane: actin-based motility of plant peroxisomes. *Canadian Journal of Botany*, 80(4):430–441, 2002.
- [11] Gaudenz Danuser. Computer vision in cell biology. *Cell*, 147(5):973–978, 2011.
- [12] J Derk森. Pollen tubes: a model system for plant cell growth. *Botanica Acta*, 109(5):341–345, 1996.
- [13] Herbert Edelsbrunner and John Harer. *Computational topology: an introduction*. American Mathematical Soc., 2010.
- [14] Gerald B Folland. *Real analysis: modern techniques and their applications*. John Wiley & Sons, 2013.
- [15] Andrew Gelman, Hal S Stern, John B Carlin, David B Dunson, Aki Vehtari, and Donald B Rubin. *Bayesian data analysis*. Chapman and Hall/CRC, 2013.
- [16] Ryan Gutierrez, Jelmer J Lindeboom, Alex R Paredez, Anne Mie C Emons, and David W Ehrhardt. Arabidopsis cortical microtubules position cellulose synthase delivery to the plasma membrane and interact with cellulose synthase trafficking compartments. *Nature cell biology*, 11(7):797, 2009.
- [17] Takahiro Hamada, Motoki Tominaga, Takashi Fukaya, Masayoshi Nakamura, Akihiko Nakano, Yuichiro Watanabe, Takashi Hashimoto, and Tobias I Baskin. Rna processing bodies, peroxisomes, golgi bodies, mitochondria, and endoplasmic reticulum tubule junctions frequently pause at cortical microtubules. *Plant and Cell Physiology*, 53(4):699–708, 2012.
- [18] Brian Herman and David F Albertini. A time-lapse video image intensification analysis of cytoplasmic organelle movements during endosome translocation. *The Journal of cell biology*, 98(2):565–576, 1984.
- [19] Michael Hirsch, Richard J Wareham, Marisa L Martin-Fernandez, Michael P Hobson, and Daniel J Rolfe. A stochastic model for electron multiplication charge-coupled devices—from theory to practice. *PloS one*, 8(1):e53671, 2013.

- [20] Bo Huang, Mark Bates, and Xiaowei Zhuang. Super-resolution fluorescence microscopy. *Annual review of biochemistry*, 78:993–1016, 2009.
- [21] Fang Huang, Tobias MP Hartwich, Felix E Rivera-Molina, Yu Lin, Whitney C Duim, Jane J Long, Pradeep D Uchil, Jordan R Myers, Michelle A Baird, Walther Mothes, et al. Video-rate nanoscopy using scmos camera-specific single-molecule localization algorithms. *Nature methods*, 10(7):653, 2013.
- [22] Anil K Jain, M Narasimha Murty, and Patrick J Flynn. Data clustering: a review. *ACM computing surveys (CSUR)*, 31(3):264–323, 1999.
- [23] James Janesick and Tom Elliott. History and advancement of large array scientific ccd imagers. In *Astronomical CCD Observing and Reduction Techniques*, volume 23, page 1, 1992.
- [24] Kai Kang, Vasileios Maroulas, and Ioannis D Schizas. Drift homotopy particle filter for non-gaussian multi-target tracking. In *17th International Conference on Information Fusion (FUSION)*, pages 1–7. IEEE, 2014.
- [25] Kai Kang, Vasileios Maroulas, Ioannis D Schizas, and Erik Blasch. A multilevel homotopy mcmc sequential monte carlo filter for multi-target tracking. In *Information Fusion (FUSION), 2016 19th International Conference on*, pages 2015–2021. IEEE, 2016.
- [26] Kody Law, Andrew Stuart, and Kostas Zygalakis. Data assimilation. *Cham, Switzerland: Springer*, 2015.
- [27] Antony Lee, Konstantinos Tsekouras, Christopher Calderon, Carlos Bustamante, and Steve Pressé. Unraveling the thousand word picture: an introduction to super-resolution data analysis. *Chemical reviews*, 117(11):7276–7330, 2017.
- [28] Jeff W Lichtman and José-Angel Conchello. Fluorescence microscopy. *Nature methods*, 2(12):910, 2005.
- [29] IK Lichtscheidl and I Foissner. Video microscopy of dynamic plant cell organelles: principles of the technique and practical application. *Journal of Microscopy*, 181(2):117–128, 1996.
- [30] Sheng Liu, Michael J Mlodzianoski, Zhenhua Hu, Yuan Ren, Kristi McElmurry, Daniel M Suter, and Fang Huang. scmos noise-correction algorithm for microscopy images. *Nature methods*, 14(8):760, 2017.
- [31] Clive W Lloyd. The plant cytoskeleton: the impact of fluorescence microscopy. *Annual Review of Plant Physiology*, 38(1):119–137, 1987.
- [32] Vasileios Maroulas, Andreas Nebenführ, et al. Tracking rapid intracellular movements: a bayesian random set approach. *The Annals of Applied Statistics*, 9(2):926–949, 2015.
- [33] Vasileios Maroulas and Panos Stinis. Improved particle filters for multi-target tracking. *Journal of Computational Physics*, 231(2):602–611, 2012.
- [34] James Munkres. *Topology*. Pearson Education, 2014.
- [35] Andreas Nebenführ. Identifying subcellular protein localization with fluorescent protein fusions after transient expression in onion epidermal cells. In *Plant Cell Morphogenesis*, pages 77–85. Springer, 2014.
- [36] Andreas Nebenführ, Larry A Gallagher, Terri G Dunahay, Jennifer A Frohlick, Anna M Mazurkiewicz, Janet B Meehl, and L Andrew Staehelin. Stop-and-go movements of plant golgi stacks are mediated by the acto-myosin system. *Plant physiology*, 121(4):1127–1141, 1999.
- [37] Brook K Nelson, Xue Cai, and Andreas Nebenführ. A multicolored set of in vivo organelle markers for co-localization studies in arabidopsis and other plants. *The Plant Journal*, 51(6):1126–1136, 2007.
- [38] Thomas D Pollard and John A Cooper. Actin, a central player in cell shape and movement. *Science*, 326(5957):1208–1212, 2009.

- [39] Lawrence R Rabiner. A tutorial on hidden markov models and selected applications in speech recognition. *Proceedings of the IEEE*, 77(2):257–286, 1989.
- [40] Markus Raffel, Christian E Willert, Fulvio Scarano, Christian J Kähler, Steve T Wereley, and Jürgen Kompenhans. *Particle image velocimetry: a practical guide*. Springer, 2018.
- [41] Ivo F Sbalzarini and Petros Koumoutsakos. Feature point tracking and trajectory analysis for video imaging in cell biology. *Journal of structural biology*, 151(2):182–195, 2005.
- [42] Ioannis Sgouralis, Andreas Nebenführ, and Vasileios Maroulas. A bayesian topological framework for the identification and reconstruction of subcellular motion. *SIAM Journal on Imaging Sciences*, 10(2):871–899, 2017.
- [43] DAVID M Shotton. Video-enhanced light microscopy and its applications in cell biology. *J Cell Sci*, 89(2):129–150, 1988.
- [44] Gurjeet Singh, Facundo Mémoli, and Gunnar E Carlsson. Topological methods for the analysis of high dimensional data sets and 3d object recognition. In *SPBG*, pages 91–100, 2007.
- [45] Ihor Smal, Katharina Draegestein, Niels Galjart, Wiro Niessen, and Erik Meijering. Particle filtering for multiple object tracking in dynamic fluorescence microscopy images: Application to microtubule growth analysis. *IEEE Transactions on Medical Imaging*, 27(6):789–804, 2008.
- [46] Ihor Smal, Wiro Niessen, and Erik Meijering. Particle filtering for multiple object tracking in molecular cell biology. In *Nonlinear Statistical Signal Processing Workshop, 2006 IEEE*, pages 129–132. IEEE, 2006.
- [47] Donald L Snyder, Abed M Hammoud, and Richard L White. Image recovery from data acquired with a charge-coupled-device camera. *JOSA A*, 10(5):1014–1023, 1993.
- [48] Edwin H Spanier. *Algebraic topology*, volume 55. Springer Science & Business Media, 1989.
- [49] Imogen A Sparkes. Motoring around the plant cell: insights from plant myosins, 2010.
- [50] Lawrence D Stone, Roy L Streit, Thomas L Corwin, and Kristine L Bell. *Bayesian multiple target tracking*. Artech House, 2013.
- [51] Julianna K Vick and Andreas Nebenführ. Putting on the breaks: Regulating organelle movements in plant cells f. *Journal of integrative plant biology*, 54(11):868–874, 2012.
- [52] Christian E Willert and Morteza Gharib. Digital particle image velocimetry. *Experiments in fluids*, 10(4):181–193, 1991.
- [53] Christopher KI Williams and Carl Edward Rasmussen. *Gaussian processes for machine learning*, volume 2. MIT Press Cambridge, MA, 2006.
- [54] Barbara Zitova and Jan Flusser. Image registration methods: a survey. *Image and vision computing*, 21(11):977–1000, 2003.